



Changes in Seismic Anisotropy Shed Light on the Nature of the Gutenberg Discontinuity

Caroline Beghein *et al.*
Science **343**, 1237 (2014);
DOI: 10.1126/science.1246724

This copy is for your personal, non-commercial use only.

If you wish to distribute this article to others, you can order high-quality copies for your colleagues, clients, or customers by [clicking here](#).

Permission to republish or repurpose articles or portions of articles can be obtained by following the guidelines [here](#).

The following resources related to this article are available online at www.sciencemag.org (this information is current as of March 13, 2014):

Updated information and services, including high-resolution figures, can be found in the online version of this article at:

<http://www.sciencemag.org/content/343/6176/1237.full.html>

Supporting Online Material can be found at:

<http://www.sciencemag.org/content/suppl/2014/02/26/science.1246724.DC1.html>

This article **cites 52 articles**, 13 of which can be accessed free:

<http://www.sciencemag.org/content/343/6176/1237.full.html#ref-list-1>

This article appears in the following **subject collections**:

Geochemistry, Geophysics

http://www.sciencemag.org/cgi/collection/geochem_phys

28. I. P. Stolarov, M. N. Vargaftik, D. I. Shishkin, I. I. Moiseev, *J. Chem. Soc. Chem. Commun.* **1991**, 938–939 (1991).
29. A. J. Bard, R. Parsons, J. Jordan, *Standard Potentials in Aqueous Solution* (International Union of Pure and Applied Chemistry, New York, 1985).
30. M. Ahlquist, R. A. Periana, W. A. Goddard III, *Chem. Commun. (Camb.)* **17**, 2373–2375 (2009).
31. F. Basolo, R. G. Pearson, *Mechanisms of Inorganic Reactions* (Wiley, New York, ed. 2, 1967).
32. R. G. Peterson, *Hard and Soft Acids and Bases* (Dowden, Hutchinson and Ross, Stroudsburg, PA, 1973).
33. H. Kurosawa, R. Okawara, *J. Organomet. Chem.* **10**, 211–217 (1967).
34. T. Fujii, K. Funahashi, I. Hirose, U.S. patent 3399956 (1968)
35. R. A. Johnson, U.S. patent 4113756 (1978)
36. R. A. Johnson, U.S. patent 4192814 (1980)

Acknowledgments: This work was supported as part of the Center for Catalytic Hydrocarbon Functionalization, an Energy Frontier Research Center Funded by the U.S. Department of Energy, Office of Science, Office of Basic Energy Sciences, under award DE-SC0001298 (to R.A.P. and D.H.E.). D.H.E. thanks the BYU Fulton Supercomputing Lab. We also thank S. Burt (BYU) for assistance with TI NMR. Several provisional and one nonprovisional patents have been filed (applications

PCT/US2014/018175, 61/768,715, 61/862,715, 61/862,723, and 61/862,731).

Supplementary Materials

www.sciencemag.org/content/343/6176/1232/suppl/DC1
Materials and Methods
Figs. S1 to S9
Tables S1 to S3
Schemes S1 to S4
References (37–47)

5 December 2013; accepted 19 February 2014
10.1126/science.1249357

Changes in Seismic Anisotropy Shed Light on the Nature of the Gutenberg Discontinuity

Caroline Beghein,^{1*} Kaiqing Yuan,¹ Nicholas Schmerr,² Zheng Xing¹

The boundary between the lithosphere and asthenosphere is associated with a platewide high-seismic velocity “lid” overlying lowered velocities, consistent with thermal models. Seismic body waves also intermittently detect a sharp velocity reduction at similar depths, the Gutenberg (G) discontinuity, which cannot be explained by temperature alone. We compared an anisotropic tomography model with detections of the G to evaluate their context and relation to the lithosphere-asthenosphere boundary (LAB). We find that the G is primarily associated with vertical changes in azimuthal anisotropy and lies above a thermally controlled LAB, implying that the two are not equivalent interfaces. The origin of the G is a result of frozen-in lithospheric structures, regional compositional variations of the mantle, or dynamically perturbed LAB.

Plate tectonic theory describes a strong and rigid lithospheric “lid” that translates coherently atop a weaker and more deformable convecting asthenosphere. Determining the depth and pervasiveness of the interface between these two layers, known as the lithosphere-asthenosphere boundary (LAB), is key for understanding the formation, evolution, and thermochemical properties of plates and associated tectonics. The exact compositional and thermal mechanisms that control this rheological division remain enigmatic, but seismological imaging of anisotropy—the directional dependence of seismic wave velocity—across the upper mantle provides an essential tool for interrogating the transition in material properties across the LAB.

Seismological interrogations of the oceanic upper mantle beneath the Pacific Ocean find evidence for a sharp drop in seismic velocity, known as the Gutenberg (G) discontinuity (1), at 40- to 100-km depth. The depth of the G roughly coincides with the top of a low-velocity zone (LVZ) and may be the seismological expression of the LAB. However, correlating G depth with plate age and distance to mid-ocean ridges has not produced a unifying interpretation of the relationship between the G and the LAB (2–6). This has led to several alternative hypotheses for

the origin of the G, including partial melt lenses in the asthenosphere (3), hydrogen depletion of olivine from decompression melting beneath mid-oceanic ridges (7, 8), frequency-dependent attenuation effects reducing the shear modulus in the presence of mantle hydration (9), and dynamical melt-producing processes to explain the strong regional variations in G reflectivity from SS precursor data (5, 10).

To improve our understanding of how isotropic and anisotropic velocity models relate to the observations of seismic discontinuities, we modeled the three-dimensional isotropic and anisotropic structure of the upper mantle beneath the Pacific Basin (Fig. 1) using a global data set of surface wave phase velocity maps (11, 12). The dispersive properties of surface waves make them ideal to put depth constraints on seismic anisotropy and velocity, and the use of higher-mode surface waves to model azimuthal anisotropy provides sensitivity throughout the upper mantle (fig. S1). The detection of changes in seismic anisotropy has been successfully used to identify layering in the mantle, variations in LAB depth beneath continents and oceans (13, 14), and chemical stratification within the lithosphere under the North American craton (14). Here we focus on anisotropy under the Pacific Plate, which is well sampled by surface waves and therefore constitutes a natural laboratory to constrain the evolution and cooling history of the oceanic lithosphere. The surface wave anisotropy results are compared to a large data set of high-frequency SS precursors that highlight the G (5).

Our models show a stratified upper mantle under the Pacific Ocean and a correlation between the boundaries of these layers and the location of observed seismic discontinuities (Fig. 2). The top layer (layer 1) is defined by a poor alignment between V_{SV} fast axes direction and the absolute plate motion (APM) (15), and the underlying layer (layer 2) by a better alignment with the APM. Layer 1 is also characterized by high seismic velocities away from ocean ridges [4 to 5% with respect to our reference model (16)], and its thickness increases with crustal age, similar to past surface wave studies (13, 17–19). Furthermore, layer 1 is associated with 1 to 2% radial anisotropy with $V_{SV} > V_{SH}$, and azimuthal anisotropy amplitudes of 1 to 2%. This fast V_{SV} direction roughly follows the orientation of ocean floor fracture zones at 50-km depth near ridges, around 80-km depth for ocean ages between 80 and 120 million years ago (Ma), and at 100-km depth under old oceanic plates (Fig. 1). Ocean floor fracture zones are temporally stable features that record plate motion path and can thus be used as proxy for the paleospreading directions. Layer 2 has lower S-wave velocity (–5% relative perturbations), strong radial anisotropy (5%) with $V_{SH} > V_{SV}$, and 3% azimuthal anisotropy with, by definition, fast axes subparallel to the APM (<30° deviation from APM).

On the basis of the above seismological observations, we define the LAB in our models as the dipping interface between these two layers. The strong anisotropy of layer 2 suggests alignment of olivine fast axes with mantle flow direction associated with plate motion that can occur in the deformable asthenosphere by dislocation creep (20) or diffusion creep (21). Olivine lattice-preferred orientation (LPO) formed by mantle flow-induced shear strain in the dislocation creep regime is consistent with a low-viscosity asthenosphere (22) and a flow channel coincident with a low-velocity zone (23). The thickness of our tomographically defined layer 1 increases with plate age, following the 900° to 1100°C isotherms in a half-space cooling (HSC) model (black lines, Fig. 2). Combined with elevated seismic velocities, layer 1 is therefore consistent with cold lithosphere that has a thermally controlled thickness and implies that the LAB is a temperature-related phenomenon. Furthermore, the alignment of the V_{SV} fast axes with the fossil spreading direction in layer 1 is consistent with LPO and the frozen-in record

¹Department of Earth, Planetary, and Space Sciences, University of California, Los Angeles, 595 Charles Young Drive East, Box 951567, Los Angeles, CA 90095–1567, USA. ²Department of Geology, University of Maryland, College Park, MD 20742, USA.

*Corresponding author. E-mail: cbeghein@ucla.edu

of past deformation in that layer for ages up to 80 Ma (13, 19, 21). For older ages, the fast axes align with the sea-floor fracture zones below 50- to 80-km depth, but they do not align with either the APM or the fossil spreading directions at shallower depths, implying that another mechanism is required to explain the observations in this depth and age range. The depth of the change in radial anisotropy from $V_{SV} > V_{SH}$ to $V_{SH} > V_{SV}$ does not display any age dependence (Fig. 2E), similar to previous observations (18); however, synthetic tests and calculation of the resolution matrix revealed that the vertical resolution of radial anisotropy models is poor (figs. S3 and S5).

Of particular interest are the vertical changes in the fast direction of azimuthal anisotropy detected by surface waves beneath the Pacific that overlap with the location of SS precursor detections (5) of seismic discontinuities (Fig. 2). For younger crustal ages (<30 Ma), detections of the G reside at 50- to 55-km depth, falling above the weaker gradient in azimuthal anisotropy fast axes orientation arising from nearly parallel APM and fossil spreading directions. We caution that resolving the details of the G at depths of <50 km is challenging for the SS precursor technique, owing to the masking of shallower complexities by the large negative sidelobe of SS (4). In addition, ridges are relatively narrow structures compared to the long-wavelength SS Fresnel zone (>1000 km) and aliasing of small-scale structure may occur across the ridge axis. Nonetheless, G detections near the ridges fall within layer 2. For crustal ages between 30 and 100 Ma, G detections coincide with both the depth of a strong change in azimuthal anisotropy and fast axes directions (Fig. 2, A and C), and lying near the base of layer 1 (55 to 70 km). Beneath 100- to 130-Ma crust, the G detections are still associated with the strong gradient in azimuthal anisotropy fast axes direction, primarily falling beneath Hawaii at 75- to 80-km depth, and are confined to the interior of layer 1. The G is poorly resolved beneath regions of crust older than 130 Ma; these regions are under-sampled by the SS precursors, with only a few sporadic detections of reflectors beneath the oldest portions of the oceanic plate (24). Thus, the G is associated with vertical changes in mantle azimuthal anisotropy.

For a discontinuity arising from anisotropy, the detection of the interface is dependent on the relative orientations of the overlying and underlying fabrics, combined with the strength of the anisotropy in each layer and the azimuthal sampling provided by source-receiver paths. As discussed in (24), layered changes in azimuthal anisotropy give rise to SS precursor underside reflections of varying amplitude and sign, depending on the relative orientation of anisotropy within each layer. Despite limitations in the resolution near ridges and a lack of data sampling beneath older crust, where observed, the detections of the G reflector are tied to vertical changes in mantle anisotropy at a roughly constant depth

(Fig. 2), thus requiring a compositional or dynamical component for the origin of the G over purely thermal mechanisms.

Partial melt in the LVZ can help explain observations of increased shear velocity contrast, attenuation (10), and mantle conductivity (25). Where the G roughly coincides with the top of layer 2, partial melt also offers a possible explanation for observations of layered anisotropy (3). Partial melt will introduce azimuthal

anisotropy when mantle flow in layer 2 entrains and segregates a small fraction of melt into en echelon tilted layers (26), with fast axes aligned perpendicular to mantle flow (Fig. 3A). The presence of such a feature would result in the formation of the G at the solidus/melt interface or where there is a change in mantle permeability (5). In this model of the G, partial melt must be long-lived and/or dynamically renewed to sustain such structures, and thus sheared

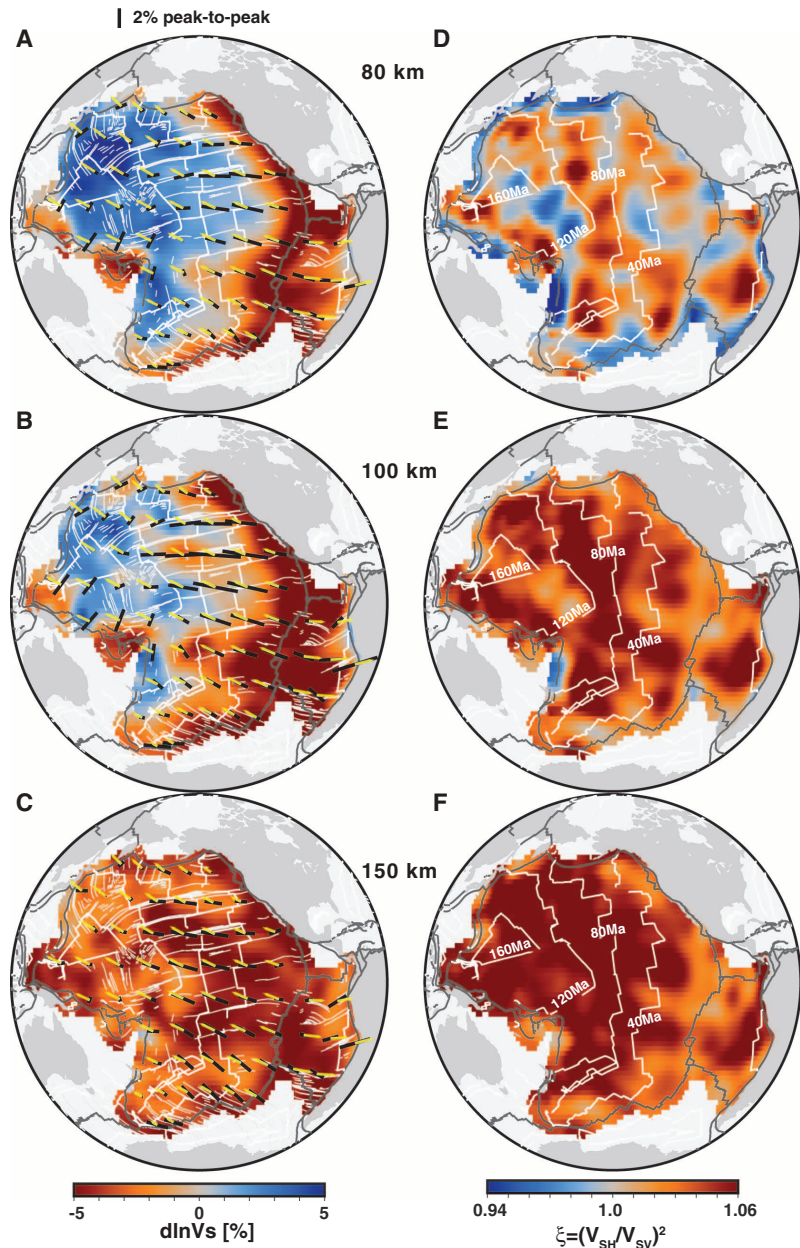


Fig. 1. Lateral variations in wave velocity and anisotropy at different depths. Mantle S-wave velocity anomalies (A to C) are given with respect to the radially anisotropic Preliminary Reference Earth Model, PREM (16). Azimuthal anisotropy is plotted on top of the velocity model with black bars representing the fast V_{SV} direction. Yellow arrows represent the APM obtained from no-net-rotation reference frame model NNR-NUVEL 1A (15), and thin white lines denote ocean floor fracture zones (27). Thick white contour lines denote ocean floor ages at 40-Ma intervals. They are annotated in (D to F), which display our radial anisotropy model. Other depths are shown in fig. S26. Considering the estimated lateral resolution of the data used, we do not resolve variations in V_S or ξ much smaller than 1600 km (and 5000 km for azimuthal anisotropy).

melt layers would be expected to produce persistent azimuthal anisotropy in the vicinity and downstream of sustained mantle upwellings (24), or in the regions of melting produced by small-scale convection. This interpretation is consistent with the observed strong azimuthal anisotropy and well-defined G detections near Hawaii, a long-lived mantle upwelling.

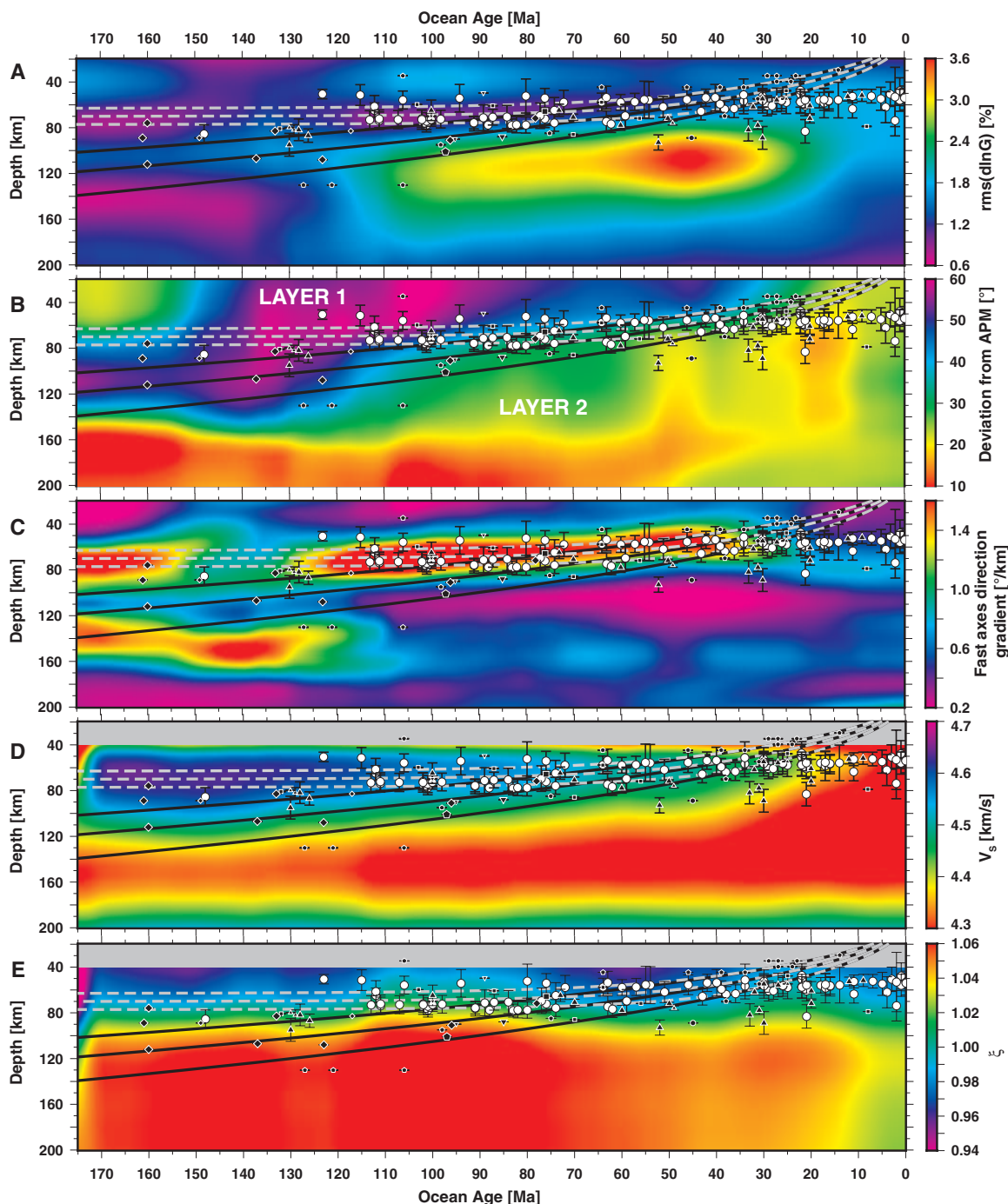
Alternatively, variable hydration with depth offers a subsolidus mechanism for producing anisotropy [e.g., (7, 9), Fig. 3B], although not necessarily in exclusion of tilted melt layers. The presence of 100- to 300-ppm (parts per million) H_2O reduces the viscosity of olivine and mod-

ifies the mineral's anisotropic properties (8), readily producing fabrics at higher hydration states and elevated temperature. Dehydration of the mantle underlying the mid-ocean ridge generates a chemically depleted, viscous layer of 50- to 80-km thickness (7) that subsequently becomes overprinted by lowered temperatures as the plate cools and migrates away from the spreading center. This will produce alignment of the olivine SV fast axes with the paleospreading direction at the ridge, occurring primarily in the underlying hydrated, and more deformable, layer 2, producing an anisotropic discontinuity at the base of the dehydrated

layer. As the lid cools and thickens, this alignment would be frozen and preserved into the part of the lithosphere (layer 1) that lies below the chemical depletion boundary, whereas flow in the warmer underlying asthenosphere (layer 2) would align with present-day APM and potentially deviate from flow at the ridge. This interpretation accounts for the anisotropy of layer 2 and for the frozen-in anisotropy observed below the G in layer 1. In this scenario, both the asthenosphere and the part of the lithosphere located below the G are hydrated, but thermal effects dominate the nature of the lid and underlying LVZ.

Fig. 2. Anisotropy and velocity models as a function of oceanic crust age.

Plate-averaged (A) azimuthal anisotropy amplitude, (B) angular difference between V_{SV} fast axes and APM directions (15), (C) vertical gradient of fast SV axes orientation, (D) S -wave velocity, and (E) radial anisotropy as a function of ocean sea-floor age beneath the Pacific. The black lines represent HSC models (28), assuming $T_m = 1350^\circ\text{C}$ for the mantle temperature and $\kappa = 10^{-6} \text{ m}^2 \text{ s}^{-1}$ for the thermal diffusivity. Gray dashed lines are for plate models (29). The temperature interval is 100°C starting at 900°C for the shallowest isotherm. The white circles and their standard deviations correspond to SS precursor detections of the G (5). Other symbols correspond to other high-frequency analyses of seismic discontinuities from other groups for whom references can be found in the caption of fig. S10.



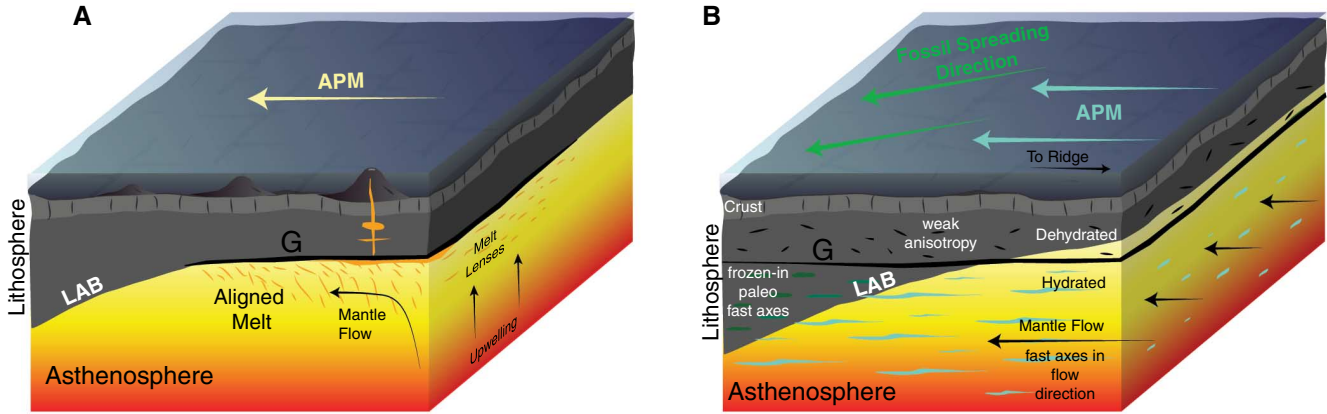


Fig. 3. Proposed models for azimuthal anisotropy beneath the Pacific and detection of the G. (A) The G as the top of an anisotropic entrainment and segregation of melt within the asthenosphere. Dynamical upwelling produces melt that is entrained into mantle flow and compacts at the base of the lithosphere from a solidus-induced change in permeability (10). The G coincides with the top of the melting zone. In the scenario where the APM and fossil spreading

directions are parallel, the G would not be detected. **(B)** The G as a chemical boundary between a weakly anisotropic dry layer and a hydrated region characterized by the fossil frozen-in alignment of olivine. Olivine aligns with the present-day APM in the hydrated, warm asthenosphere. In this scenario, G can be both coincident with and above the thermally defined LAB and is detected by the SS precursors where the anisotropy contrast between the two layers is large.

References and Notes

1. B. Gutenberg, *Bull. Seismol. Soc. Am.* **38**, 121 (1948).
2. B. Bagley, J. Revenaugh, *J. Geophys. Res. Solid Earth* **113**, B12301 (2008).
3. H. Kawakatsu *et al.*, *Science* **324**, 499–502 (2009).
4. C. A. Rychert, P. M. Shearer, *J. Geophys. Res. Solid Earth* **116**, B07307 (2011).
5. N. Schmerr, *Science* **335**, 1480–1483 (2012).
6. Y. Tan, D. V. Helmberger, *J. Geophys. Res. Solid Earth* **112**, B08301 (2007).
7. J. B. Gaherty, M. Kato, T. H. Jordan, *Phys. Earth Planet. Inter.* **110**, 21–41 (1999).
8. G. Hirth, D. L. Kohlstedt, *Earth Planet. Sci. Lett.* **144**, 93–108 (1996).
9. S. Karato, *Earth Planet. Sci. Lett.* **321–322**, 95–103 (2012).
10. T. Sakamaki *et al.*, *Nat. Geosci.* **6**, 1041–1044 (2013).
11. Materials and methods are available on Science Online.
12. K. Visser, J. Trampert, B. L. N. Kennett, *Geophys. J. Int.* **172**, 1016–1032 (2008).
13. E. Debayle, Y. Ricard, *Earth Planet. Sci. Lett.* **376**, 165–177 (2013).
14. H. Yuan, B. Romanowicz, *Nature* **466**, 1063–1068 (2010).
15. A. E. Gripp, R. G. Gordon, *Geophys. J. Int.* **150**, 321–361 (2002).
16. A. M. Dziewonski, D. L. Anderson, *Phys. Earth Planet. Inter.* **25**, 297–356 (1981).
17. A. Maggi, E. Debayle, K. Priestley, G. Barruol, *Geophys. J. Int.* **166**, 1384–1397 (2006).
18. M. Nettles, A. M. Dziewonski, *J. Geophys. Res. Solid Earth* **113**, B02303 (2008).
19. C. E. Nishimura, D. W. Forsyth, *Geophys. J.* **96**, 203–229 (1989).
20. S. Karato, in *High-Pressure Research in Mineral Physics*, M. H. Manghni, Y. Syono, Eds. (TERRAPUB/AGU, Tokyo/Washington, 1987), pp. 455–471.
21. T. Miyazaki, K. Sueyoshi, T. Hiraga, *Nature* **502**, 321–326 (2013).
22. B. H. Hager, M. A. Richards, *Philos. Trans. R. Soc. Lond. A* **328**, 309–327 (1989).
23. C. Gaboret, A. M. Forte, J. P. Montagner, *Earth Planet. Sci. Lett.* **208**, 219–233 (2003).
24. C. A. Rychert, N. Schmerr, N. Harmon, *Geochem. Geophys. Geosyst.* **13**, Q0AK10 (2012).
25. S. Naif, K. Key, S. Constable, R. L. Evans, *Nature* **495**, 356–359 (2013).
26. B. K. Holtzman, J. M. Kendall, *Geochem. Geophys. Geosyst.* **11**, Q0AB06 (2010).

27. K. J. Matthews, R. D. Muller, P. Wessel, J. M. Whittaker, *J. Geophys. Res. Solid Earth* **116**, B12109 (2011).
28. R. L. Parker, D. W. Oldenburg, *Nature* **242**, 137–139 (1973).
29. C. A. Stein, S. Stein, *Nature* **359**, 123–129 (1992).

Acknowledgments: C.B. and K.Y. were funded by NSF EAR grants 0838605 and 0949255; N.S. was funded by NSF EAR 1247608. We thank J. Trampert and K. Visser for making their phase velocity maps freely available. Partial derivatives were calculated using fortran code MINEOS (www.geodynamics.org/cig/software/mineos), and figures were made with the Generic Mapping Tools, Gnuplot, and Xmgrace. We thank P. Davis for fruitful discussions. The data used were the phase velocity maps published in (12) and

are available at www.geo.uu.nl/~jeannot/My_web_pages/Downloads.html. The models are available in the supplementary materials.

Supplementary Materials
www.sciencemag.org/content/343/6176/1237/suppl/DC1
 Materials and Methods
 Supplementary Text
 Figs. S1 to S27
 Table S1
 References (30–56)
 Model file S1

2 October 2013; accepted 17 February 2014
 Published online 27 February 2014;
 10.1126/science.1246724

Lethal Interactions Between Parasites and Prey Increase Niche Diversity in a Tropical Community

Marty A. Condon,^{1*} Sonja J. Scheffer,² Matthew L. Lewis,² Robert Wharton,³ Dean C. Adams,^{4,5} Andrew A. Forbes⁶

Ecological specialization should minimize niche overlap, yet herbivorous neotropical flies (*Blepharoneura*) and their lethal parasitic wasps (parasitoids) exhibit both extreme specialization and apparent niche overlap in host plants. From just two plant species at one site in Peru, we collected 3636 flowers yielding 1478 fly pupae representing 14 *Blepharoneura* fly species, 18 parasitoid species (14 *Bellopius* species), and parasitoid-host associations, all discovered through analysis of molecular data. Multiple sympatric species specialize on the same sex flowers of the same fly host-plant species—which suggests extreme niche overlap; however, niche partitioning was exposed by interactions between wasps and flies. Most *Bellopius* species emerged as adults from only one fly species, yet evidence from pupae (preadult emergence samples) show that most *Bellopius* also attacked additional fly species but never emerged as adults from those flies.

Plant and insect diversity both peak in the tropics (1) where insect diversity is strongly associated with plant diversity (2, 3) and extreme specialization (4). Ecological specialization is often considered a driver of diversification, with increasing specialization reducing niche over-

lap and promoting speciation (5, 6). Diversification of herbivorous insects, arguably the most diverse group of organisms on Earth (7), is often explained by “arms race” or “escape and radiate” hypotheses involving specialized interactions either between two trophic levels—host plants and